Research Article Vol. 38, No. 4 / April 2021 / Journal of the Optical Society of America B 1405

Journal of the Optical Society of America B

OPTICAL PHYSICS

Sensitivity enhancement of a difference interferometer refractive index sensor based on a silicon-on-insulator hybrid plasmonic waveguide

HESHAM A. OKDA,[1,2,*] SHERIF I. RABIA,[2,3] AND HOSSAM M. H. SHALABY[1,4]

[1]Electronics and Communications Engineering (ECE) Department, Egypt-Japan University of Science and Technology (E-JUST), Alexandria 21934, Egypt
[2]Department of Engineering Mathematics and Physics, Faculty of Engineering, Alexandria University, Alexandria 21544, Egypt
[3]Basic and Applied Sciences (BAS) Institute, Egypt-Japan University of Science and Technology (E-JUST), Alexandria 21934, Egypt
[4]Electrical Engineering Department, Faculty of Engineering, Alexandria University, Alexandria 21544, Egypt
*Corresponding author: hesham@alexu.edu.eg

Received 21 January 2021; revised 26 February 2021; accepted 9 March 2021; posted 9 March 2021 (Doc. ID 420051); published 31 March 2021

A refractive index (RI) sensor using a silicon-on-insulator hybrid plasmonic waveguide (HPWG) difference interferometer is proposed. We first provide a rigorous analysis that enables the construction of the modal characteristic equations of the TM- and TE-polarized modes in a HPWG. These equations are solved to get the modes' complex effective indices in addition to their electromagnetic power distributions. The feature of polarization spatial diversity in HPWGs is then exploited to design a difference interferometer with a superior sensing capability. Our results reveal that the proposed device has a lower limit of detection of 1.32×10^{-6} refractive index unit (RIU) and a sensitivity of 756.2π rad/RIU at a wavelength of 1550 nm, accounting for a greater than 50% improvement to the sensitivities of recently published all-dielectric interferometers. Moreover, the sensing interactive length in this work is shown to be 1396 μm, acquiring more than a threefold reduction compared to those reported in the literature. In addition, the propagation loss is reduced by more than 5×10^2 times compared to its value in the case of a surface plasmon interferometer, which is found to enhance the detectable power level by 13.6 dB. Furthermore, the proposed HPWG difference interferometer is investigated with a broadband interrogation. Our findings come out with a high density of local extrema of the light interference intensity, for a short sensing interactive length, in the spectral range of interest (from 1490 to 1610 nm), which is favorable for accurate statistical analysis of the interference intensity signal.

https://doi.org/10.1364/JOSAB.420051

1. INTRODUCTION

Over the last two decades, silicon (Si) photonics technology has gained increasing attention to realize the integration of optical and electronic components on Si-on-insulator (SOI) wafers, based on the well-established complementary metal–oxide–semiconductor (CMOS) platform [1,2]. However, one of the most critical challenges is the demand to overcome the diffraction limit of light to reduce the dimensions of the optical building blocks down to subwavelength scale, which subsequently leads to an improved photonics integration density [3,4].

In the meantime, it is the heyday for research on plasmonics [5]. Basically, surface plasmon polaritons (SPPs) are evanescent electromagnetic waves propagating along a dielectric-metal interface. These waves are excited in response to energy coupling between an incident light and free electron oscillations in the metal at a resonant wavelength [6]. In spite of being confined at subwavelength distances in both dielectric and metal extents, surface plasmon waves primarily suffer from considerably high propagation losses, which is the main drawback of plasmonic integrated devices [7–10].

In an attempt to merge both advantages of photonics (low propagation loss) and plasmonics (nanoscale field confinement), the hybrid plasmonic waveguide (HPWG) has been reported for the first time by Alam *et al*. [11]. Generally speaking, Si HPWGs are formed by separating a high-index core layer (Si) from a metallic layer by a lower-index dielectric spacer. Different configurations of HPWGs, besides their diverse applications, have been reviewed in [12,13].

In [14–16], the authors have provided mathematical analyses for slab HPWGs, seeking to understand the nature of hybrid modes and their characteristics. In this context, we report some concerns about the previously proposed analyses, which will be treated in the present work.

Overall, we have noticed that the previously proposed analyses are restricted to hybrid transverse-magnetic (TM) modes. However, HPWGs can also support lossy transverse-electric (TE) modes that must be investigated analytically when employed in applications. Moreover, no explicit method has been given to normalize optical power transmitted by each mode to a constant value. Power normalization is essential to compare the amplitudes of propagating modes in the different layers of the waveguide. In addition, the introduced analyses in [14,15] are limited to four-layered HPWGs; that is, the metallic layer has been assumed to extend infinitely. Indeed, this assumption is not viable for various applications that employ relatively thin metallic films because the evanescent field penetrating the metal is not negligible in such cases. Furthermore, although the analysis proposed in [16] can be generalized for an arbitrary number of layers, it lacks simplicity when solving the characteristic equation of hybrid TM modes since it depends on two sequential algorithms to locate its complex roots.

At the level of applications, HPWGs can be employed to introduce novel and highly sensitive refractive index (RI) sensors because of their ability to concentrate light in the sensing region with a relatively low propagation loss [12]. Modal interferometry is a promising approach for biochemical sensing based on HPWGs. Typically, a polarized beam is split into the two channels of a Mach–Zehnder interferometer (MZI). If the RI varies in the sensing region (spacer) of the HPWG that exists on the sensing channel, the propagation constant of the mode propagating through that channel will differ from that of the propagating mode through the reference channel. Hence, a relative phase difference between the two modes will accumulate along the sensing interactive length until reaching the MZI combiner section [17]. In most recent interferometric-based sensing applications, a sensor's response is preferably obtained through a band of wavelengths instead of measuring the interference intensity pattern at a monochromatic wavelength because of the enhanced performance regarding the interferometric signal ambiguity and fading at detection. Accordingly, the sensitivity is typically expressed in terms of the wavelength shift in the transmission spectrum (nm) per refractive index unit (RIU) [18–20].

In [21], the authors have proposed a highly sensitive liquid sensor (1061 nm/RIU) based on an MZI with a double-slot HPWG. Moreover, Alam *et al*. have provided an analytical investigation of dual-polarization biosensing measurements using an MZI with HPWGs [22]. By exploiting both TM and TE polarizations together, they have illustrated how to obtain simultaneous measurements for small variations in both RI and the thickness of a solution containing biomolecules. It should be noted that such reported double-path waveguide interferometers require the MZI reference channel to be isolated so it is not affected by RI variations. In other words, the sensing region does not include the reference channel [17].

Another less studied kind of interferometric optical sensors is the difference interferometer [17]. It has a working principle similar to that of the aforementioned double-path interferometer, except that two modes of perpendicular polarizations (TE_0 and TM_0) are excited coherently and propagate through the same waveguide. Since the two orthogonal modes interact differently with the sensing medium, their accumulated phase changes along the sensing interactive length are not equal. The interferometer's response in this case is the time-dependent phase difference between the two modes, which can be experimentally measured with a high precision that reaches $2\pi \times 5 \times 10^{-4}$ rad at a temporal sampling rate of 1 ms, as explained in detail in [23].

Difference interferometers based on all-dielectric waveguide structures have been reported in a few early publications as humidity sensors, chemical refractometers, and biosensors [24–27]. The lower limit of detection (LOD) attained by this kind of sensor has been measured to be as small as 2×10^{-8} RIU; however, this comes at the expense of the long sensing interactive length that may reach up to several centimeters [28]. Recently, K. Gut theoretically proposed an alternative approach to measure a difference interferometer's response in a broadband wavelength domain [29,30]. The highest resolution presented in his work is 10^{-3} RIU, which is still very far from that obtained using the traditional phase-difference measurement.

Although it has been shown that difference interferometers have the advantages of accurate phase-difference measurement, high resolution, and high stability [28], a modified version of such interferometric devices, called bimodal waveguide (BiMW) interferometers, have been more common [17]. The working principle of a BiMW is that it relies on the unequal propagation phase changes of two modes of the same polarization but dissimilar orders (e.g., TE_0 and TE_1). A BiMW interferometer consists of a central bimodal section between input and output single-mode sections. The higher-order mode is indirectly excited in the bimodal section as a result of a partial coupling of the fundamental mode through a vertical or a horizontal asymmetric junction. BiMW interferometers have been introduced in accordance with the fact that, in conventional dielectric waveguides, a higher-order mode has more evanescent field interacting with the sensing region. In this way, the device can be miniaturized by reducing its sensing interactive length, while still keeping a high sensitivity. A BiMW interferometer's response can be easily obtained by intensity measurement; that is, the time-dependent phase difference modulates the output power of a photodetector at a certain wavelength. Alternatively, it can be measured by evaluating the spectral shifts in the wavelength domain. Generally, for the ultimate measurement accuracy, the interference pattern of the modes should be kept highly contrasting. This can be achieved by appropriately designing the BiMW interferometer with proper dimensions that will lead to identical intensity levels for both the fundamental and higher-order modes.

A variety of RI sensing applications have successfully employed BiMW interferometers. For example, in [31], the authors have demonstrated the performance of a silicon nitride (Si_3N_4)-based biosensor, showing a sensitivity of 2026 rad/RIU and an LOD of 2.5×10^{-7} RIU achieved through a 15-mm sensing interactive length. In addition, a two-lateral-modes spiral waveguide has been reported as an SOI-based biochemical sensor in [32]. The device sensitivity is 461.6π rad/RIU with a sensing interactive length of 4582 μm. In recent times, Y. Liang *et al*. have investigated a BiMW interferometer RI sensor based on a polymer (OrmoCore) platform [33]. Their results exhibit a sensitivity of 316π rad/RIU through a 5 mm

sensing interactive length. In addition, an SOI-based surface plasmon interferometer has been proposed and investigated analytically in [34], where the interference occurs between two surface plasmon modes. It has been shown that a sufficiently small LOD (1×10^{-6} RIU) can be theoretically obtained with a significantly reduced sensing interactive length (10 μm). However, the calculated propagation loss is considerably high (1.79 dB/μm), and consequently the displayed transmission does not exceed −15 dBm.

From the previous review, one can notice the promising performance of the difference interferometers as integrated RI sensors of a high resolution, along with the continuous efforts that have been made to miniaturize their sizes.

In this paper, a difference interferometer based on an SOI HPWG is demonstrated and investigated analytically. We provide a comprehensive analysis of wave propagation in planar HPWGs, which has one advantage of being valid for both TM and TE modes; yet, it relies on a simple procedure to locate the complex propagation constants of the modes using a relatively low computational power. Based on the introduced analytical approach, the HPWG difference interferometer is designed and examined in both cases of single-wavelength and broadband interrogation. The proposed interferometer is shown to achieve the optimal balance between the long sensing interactive lengths of all-dielectric single-path interferometers and the excessive propagation losses of plasmonic ones. In addition, when employed with a broadband source, the HPWG difference interferometer can offer a higher degree of accuracy to resolve the detectable light interference pattern, compared to the all-dielectric broadband difference interferometers.

This paper has a total of five sections. The structure of the proposed HPWG difference interferometer is described in Section 2. Section 3 is devoted for the theoretical analysis of wave propagation in HPWGs. The obtained results are presented and discussed in Section 4. Our concluding remarks are presented in Section 5.

2. STRUCTURE OF THE HPWG DIFFERENCE INTERFEROMETER

Figure 1 shows a schematic of the proposed SOI-based HPWG difference interferometer. It consists of a slab HPWG with an Si core layer of thickness t_1 on a lower silica (SiO_2) buried oxide (BOX) layer. The sensing region is the spacer of thickness t_2 that provides a small separation between the Si layer and an upper silver (Ag) film of thickness t_3 cladded by SiO_2. The spacer in this structure is a nanofluidic channel through which a liquid or a gas (sensing medium) passes to detect perturbations in its RI n_s. Throughout this work, the unperturbed sensing medium is assumed to be a liquid of a RI $n_s' = 1.33$. The, assuming a central operating wavelength $\lambda_c = 1550$ nm, the RIs of Si and SiO_2 are obtained to be 3.47 and 1.44, respectively [1]; Ag has an RI of $0.14 + j11.31$ [35]. Here, an Ag film is considered because it has been shown that silver is superior in terms of the relatively low absorptivity near the central operating wavelength compared to the rest of the common plasmonic metals [36].

In principle, the two orthogonal polarizations, represented by the modes TM_0 and TE_0, propagate along the z direction and interact differently with the sensing medium, accumulating

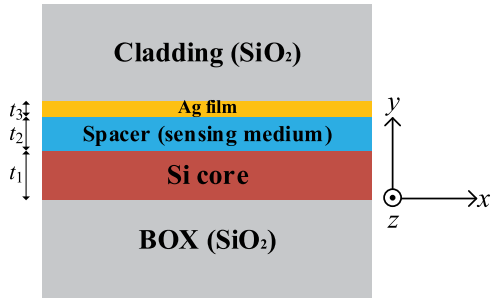

Fig. 1. Schematic of SOI-based HPWG difference interferometer. The coordinate system used in this paper is also shown.

unequal phase changes during propagation. A small variation δn_s in the RI of the sensing medium (spacer) will generate a resultant shift in the phase difference between the two modes, which can be expressed as [24,25]

$$\delta\Delta\phi = \frac{2\pi}{\lambda_c} L \times \left(\frac{\partial n_{\text{eff,TM}_0}}{\partial n_s} - \frac{\partial n_{\text{eff,TE}_0}}{\partial n_s} \right)\Big|_{n_s'} \delta n_s, \quad (1)$$

where L is the sensing interactive length; $n_{\text{eff,TM}_0}$ and $n_{\text{eff,TE}_0}$ are the effective indices of TM_0 and TE_0, respectively.

At the waveguide output, light from the two orthogonal modes TM_0 and TE_0 is passed through a polarizer aligned at 45° so as to bring half the optical power to one common polarization. The produced light intensity is being modulated by the time-varying phase difference that depends on the variation in n_s.

Nonetheless, as mentioned in Section 1, interrogating such an interferometric sensor by a broad-spectrum light source is demanded, especially when a wide dynamic range of RI variations is required to be detectable unambiguously. Assuming that the two modes are launched at the waveguide input with an equal intensity distributive function $I_0(\lambda)$, we derive an expression for the light interference intensity $I(\lambda)$ in the case of our proposed HPWG difference interferometer as

$$I(\lambda) = \frac{1}{2} I_0(\lambda) e^{-\Im\left\{\beta_{\text{TM}_0}(\lambda)+\beta_{\text{TE}_0}(\lambda)\right\}L} \times \left(\cosh\left[\Im\left\{\Delta\beta(\lambda)\right\}L\right] + \cos\left[\Re\left\{\Delta\beta(\lambda)\right\}L\right]\right), \quad (2)$$

where $\beta_{\text{TM}_0}(\lambda)$ and $\beta_{\text{TE}_0}(\lambda)$, respectively, are the complex propagation constants of TM_0 and TE_0 as functions of wavelength λ; and $\Delta\beta(\lambda) = \beta_{\text{TE}_0}(\lambda) - \beta_{\text{TM}_0}(\lambda)$.

It is worth noticing that, by setting $\Im\{\beta_{\text{TM}_0}(\lambda)\}$ and $\Im\{\beta_{\text{TE}_0}(\lambda)\}$ to zero in Eq. (2), it reduces to that reported in [29,30] for all-dielectric broadband difference interferometers, in which $\beta_{\text{TM}_0}(\lambda)$ and $\beta_{\text{TE}_0}(\lambda)$ are both purely real-valued.

The variation δn_s leads to either a blue-shift or a red-shift in the interference spectrum. The wavelength shift of a local extremum existing at a certain wavelength λ_m in the spectrum can be approximated by the relation [18,30]

$$\delta\lambda \approx -\delta n_s \times \frac{\left(\frac{\partial\Re\{\Delta\beta\}}{\partial n_s}\right)}{\left(\frac{\partial\Re\{\Delta\beta\}}{\partial\lambda}\right)}\Big|_{\lambda_m}. \quad (3)$$

3. THEORETICAL ANALYSIS

Considering the harmonic time and longitudinal variations of the form $e^{-j(\omega t-\beta z)}$, the distribution of the transverse field component $\psi(y)$ of a certain mode in the successive layers of the HPWG can be derived as

$$\psi(y)=\begin{cases} A_1 e^{w_1 y}; & \text{BOX } (SiO_2),\\ A_i e^{w_i y}+B_i e^{-w_i y}; & \text{Inner layers, } i\in\{2,3,4\},\\ B_5 e^{-w_5 y}; & \text{Upper cladding } (SiO_2),\end{cases} \tag{4}$$

where $\psi(y)$ represents the transverse magnetic field $H_x(y)$ in the case of the TM modes, and the transverse electric field $E_x(y)$ in the case of the TE modes, $w_i=\sqrt{\beta^2-n_i^2k_0^2}$ for $i\in\{1,2,\ldots,5\}$, β is the mode complex propagation constant, n_i is the RI of layer i, and k_0 is the free-space wave number ($k_0=2\pi/\lambda$). Here, $A_i, i\in\{1,2,3,4\}$, and $B_i, i\in\{2,3,4,5\}$, are arbitrary field complex amplitudes determining the power transmitted by each mode. The inner layers $i\in\{2,3,4\}$ are the Si core, spacer, and Ag film, respectively.

For the TM modes, the associated electric field components $E_y(y)$ and $E_z(y)$ can be found from the relations

$$E_y(y)=-\frac{\beta}{\omega\epsilon_0 n_i^2}H_x(y),\qquad E_z(y)=-\frac{1}{j\omega\epsilon_0 n_i^2}\frac{\partial H_x(y)}{\partial y}, \tag{5}$$

where ω is the wave angular frequency, ϵ_0 is the free-space permittivity, and $i\in\{1,2,\ldots,5\}$.

Similarly, the magnetic field components of the TE modes can be derived through

$$H_y(y)=\frac{\beta}{\omega\mu_0}E_x(y),\qquad H_z(y)=-\frac{1}{j\omega\mu_0}\frac{\partial E_x(y)}{\partial y}, \tag{6}$$

where μ_0 is the free-space permeability.

Applying the well-known boundary conditions on the field tangential components (H_x and E_z for TM modes; E_x and H_z for TE modes) at the successive interfaces, we get a system of eight homogeneous equations in eight unknowns A_i, $i\in\{1,2,3,4\}$, and $B_i, i\in\{2,3,4,5\}$, which can be written in the following matrix form,

$$\mathbf{M}\cdot\mathbf{A}=\mathbf{0}, \tag{7}$$

where $\mathbf{M}$ is the coefficient matrix, defined by Eq. (8), and $\mathbf{A}$ is a column vector containing the field complex amplitudes A_i, $i\in\{1,2,3,4\}$, and B_i, $i\in\{2,3,4,5\}$, respectively. The coefficient matrix is

$$\mathbf{M}=\begin{bmatrix} 1 & -1 & 0 & 0 & -1 & 0 & 0 & 0\\ \kappa_1 w_1 & -\kappa_2 w_2 & 0 & 0 & \kappa_2 w_2 & 0 & 0 & 0\\ 0 & e^{w_2 t_1} & -e^{w_3 t_1} & 0 & e^{-w_2 t_1} & -e^{-w_3 t_1} & 0 & 0\\ 0 & \kappa_2 w_2 e^{w_2 t_1} & -\kappa_3 w_3 e^{w_3 t_1} & 0 & -\kappa_2 w_2 e^{-w_2 t_1} & \kappa_3 w_3 e^{-w_3 t_1} & 0 & 0\\ 0 & 0 & e^{w_3(t_1+t_2)} & -e^{w_4(t_1+t_2)} & 0 & e^{-w_3(t_1+t_2)} & -e^{-w_4(t_1+t_2)} & 0\\ 0 & 0 & \kappa_3 w_3 e^{w_3(t_1+t_2)} & -\kappa_4 w_4 e^{w_4(t_1+t_2)} & 0 & -\kappa_3 w_3 e^{-w_3(t_1+t_2)} & \kappa_4 w_4 e^{-w_4(t_1+t_2)} & 0\\ 0 & 0 & 0 & e^{w_4(t_1+t_2+t_3)} & 0 & 0 & e^{-w_4(t_1+t_2+t_3)} & -e^{-w_5(t_1+t_2+t_3)}\\ 0 & 0 & 0 & \kappa_4 w_4 e^{w_4(t_1+t_2+t_3)} & 0 & 0 & -\kappa_4 w_4 e^{-w_4(t_1+t_2+t_3)} & \kappa_5 w_5 e^{-w_5(t_1+t_2+t_3)}\end{bmatrix}. \tag{8}$$

In Eq. (8), we have

$$\kappa_i=\begin{cases}\frac{1}{n_i^2}; & \text{TM modes, } i\in\{1,2,\ldots,5\}.\\ 1; & \text{TE modes.}\end{cases} \tag{9}$$

Equation (7) has nontrivial solutions as long as it represents a linearly dependent set of equations. Accordingly, by equating the determinant of the coefficient matrix $\mathbf{M}$ to zero, the characteristic equations of the TM and TE modes are constructed and solved separately by using the *vpasolve* function in Matlab. This function locates the complex roots of each characteristic equation, producing the proper propagation constants of the supported modes.

The field complex amplitudes of each mode are found as follows. The linearly dependent set in Eq. (7) (after substituting with the proper values of β) is solved using the Matlab's symbolic toolbox to express A_i, $i\in\{1,2,3,4\}$, and B_i, $i\in\{2,3,4\}$, in terms of B_5. Therefore, $\psi(y)$ can be expressed in terms of another function $\zeta(y)$ as

$$\psi(y)=B_5\zeta(y). \tag{10}$$

Here, the choice of B_5 is optional because it can be arbitrarily replaced with any of the other constants to express the remaining field complex amplitudes in the same manner.

Next, the value of B_5 is obtained by the following relation so that mode field corresponds to a normalized power flow (through z direction) of one watt per unit width in the x direction:

$$|B_5|=\sqrt{\frac{2}{\int_{\text{waveguide layers}}\Re\{\alpha|\zeta(y)|^2\}\mathrm{d}y}}, \tag{11}$$

where

$$\alpha=\begin{cases}\frac{\beta}{\omega\epsilon_0 n_i^2}; & \text{TM modes, } i\in\{1,2,\ldots,5\},\\ \frac{\beta}{\omega\mu_0}; & \text{TE modes.}\end{cases} \tag{12}$$

In Eq. (11), the integration extends through the whole cross section of the HPWG. Therefore, it should be divided into subintegrals with the proper expressions of $\zeta(y)$ in the successive layers of the waveguide. The results of the subintegrals are then summed up to produce the end result.

It should be noted that, when solving the characteristic equations for guided modes, the following stringent condition on solution range of β is imposed:

$$k_0\max\{n_{SiO_2},n_s\}<\Re\{\beta\}<k_0 n_{Si}. \tag{13}$$

However, since only the fundamental modes TM_0 and TE_0 are exploited in our HPWG difference interferometer, we are interested in the corresponding β of the highest value when solving for each polarization.

The effective index n_{eff} and propagation length L_p of each mode can be easily obtained through

$$n_{\text{eff}} = \frac{\Re\{\beta\}}{k_0}, \qquad L_{\text{p}} = \frac{1}{2\Im\{\beta\}}. \tag{14}$$

In addition, the propagation loss Γ due to electromagnetic power absorption by Ag film is expressed in decibels per unit length as

$$\Gamma_{\text{dB}} = 20\Im\{\beta\}\log e. \tag{15}$$

4. RESULTS AND DISCUSSION

The operation principle of the proposed interferometer relies mainly on exploiting the distinct properties of the TM and TE polarizations. In contrast to all-dielectric waveguides that support only dielectric modes, the HPWG shown in Fig. 1 supports hybrid TM modes as well as lossy TE modes. The hybrid TM modes arise from the coupling of the dielectric TM modes, which are originally guided in Si core, with the surface plasmons that exist at the Ag–spacer interface, resulting in optical power spreading through the dielectric spacer medium. On the other hand, the lossy TE modes cannot be coupled with the surface plasmons because of their boundary conditions; consequently, these modes remain concentrated in the Si core and suffer from less absorptive loss induced by the Ag film.

To illustrate the difference in nature between the two types of modes, we employ Eqs. (4) and (5) to obtain the profiles of the principal electric field components $E_y(y)$ and $E_x(y)$ of TM_0 and TE_0, respectively, which are displayed in Fig. 2. For the sake of simulation, we assume t_1, t_2, and t_3 are 220 nm, 80 nm, and 15 nm, respectively, and $\lambda = \lambda_c$. Obviously, the TM_0 main lobe is shared between the Si core and spacer, whereas TE_0 is mainly confined inside the Si core. This feature is referred to as polarization spatial diversity in HPWGs, which allows us to control the characteristics of each polarization separately with more flexibility. As a validation of our proposed mathematical model, we use the same waveguide parameters in the Lumerical MODE solver to derive the profiles numerically. It is worth noticing the fair agreement between both the numerical and analytical simulations.

In what follows, we use an analytical approach, based on the presented mathematical model, because it provides accurate solutions for electromagnetic wave propagation in one-dimensional HPWGs. Meanwhile, the analytical-based solution offers one more advantage: the relative simplicity in tuning simulation parameters to help us investigate various factors in a reasonably comprehensive manner, to achieve the best performance of the proposed interferometer. We start our investigation of the HPWG difference interferometer with a single-wavelength interrogation at $\lambda_c = 1550$ nm, which is assumed to be the central operating wavelength in this work. However, by the end of this work, we expand our analysis to the broadband HPWG difference interferometer.

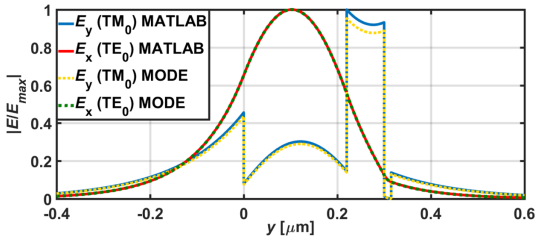

Fig. 2. Principal electric field components of hybrid mode TM_0 and lossy mode TE_0 derived analytically and numerically.

A. Effect of Ag Film Thickness on Modal Characteristics

As shown by Eq. (1), the sensitivity of the proposed interferometer $\frac{\partial \Delta\phi}{\partial n_s}$ is linearly proportional to the sensing interactive length L that should not exceed either propagation length of TM_0 ($L_{\text{p,TM}_0}$) or TE_0 ($L_{\text{p,TE}_0}$) to maintain a sufficiently detectable power level. Generally, the mode propagation length can be increased by reducing the propagation loss that mainly arises from the existence of metals in waveguiding structures. Accordingly, we aim to investigate the influence of the Ag film thickness t_3 on the electromagnetic fields as well as the associated modal characteristics of TM_0 and TE_0.

First, Eqs. (4) and (5) are employed to plot $E_y(y)$ and $E_x(y)$ of the two modes, respectively, at different values of t_3 in Fig. 3, keeping the propagating power of each mode normalized at 1 W/m using Eq. (11). For the sake of simulation, t_1 and t_2 are set to 220 nm and 80 nm, respectively. It can be noticed that, owing to the orthogonality of the TM_0 principal electric field component E_y on Ag film, this mode can excite surface plasmons that induce field intensity peaks at both film interfaces, in contrast to TE_0. Moreover, because of the electromagnetic power dissipation in Ag film, the electric field decays rapidly across it. Accordingly, as the Ag film thickness increases, a less evanescent field of TM_0 penetrates to be coupled with surface plasmons at the Ag-SiO_2 cladding interface. As a result, the field becomes less bound to the Ag film, as can be readily seen from Fig. 3(a) by noticing the decreasing electric field amplitudes at both Ag film interfaces when increasing its thickness. In this context, we point out that the hybrid mode TM_0 behaves like SPP even modes excited in insulator–metal–insulator heterostructures, in which a thin metallic layer is sandwiched between two thick dielectric claddings. In such structures, SPP even modes are less confined to metallic layers of a greater thickness [6].

Next, in Fig. 4, we depict the variations of effective indices $n_{\text{eff,TM}_0}$ and $n_{\text{eff,TE}_0}$ as well as propagation lengths $L_{\text{p,TM}_0}$ and $L_{\text{p,TE}_0}$ versus t_3 by solving the modal characteristic equations, as described above, and making use of Eq. (14). Evidently, because of the very small real part of Ag film RI, $n_{\text{eff,TM}_0}$, and $n_{\text{eff,TE}_0}$ barely decreases as t_3 increases, stabilizing at 2.19 and 2.79, respectively. Conversely, $L_{\text{p,TM}_0}$ and $L_{\text{p,TE}_0}$ grow gradually with increasing t_3, approaching 240 nm and 390 nm, respectively. The shown curves of propagation lengths reflect the fact that the propagation losses of the two modes diminish as the Ag film gets thicker. Strictly speaking, although a greater portion of the mode field extends through the Ag films of a greater thickness, this portion is invariably small, because of the rapidly decaying mode profile, to dominantly affect the mode propagation loss. Oppositely, the amount of propagation loss is dominated by mode field intensity adjacent to the film. The insets of Figs. 3(a) and 3(b) show that, as t_3 increases, both TM_0 and TE_0 exhibit noticeably less field intensities in the upper cladding near the film. As a result, the two modes become less affected by the Ag film, and their propagation lengths increase.

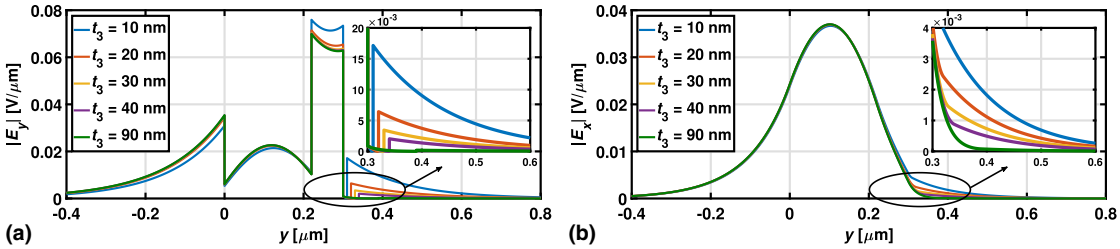

Fig. 3. Principal electric field profiles: (a) TM_0 and (b) TE_0 for various Ag film thicknesses t_3.

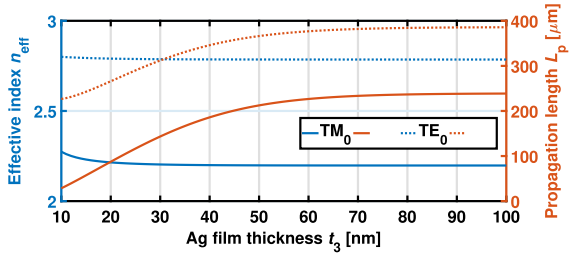

Fig. 4. Effective indices and propagation lengths of TM_0 and TE_0 with sweeping Ag film thickness t_3.

It is worth noticing the marginal influence of changing the Ag film thickness on both of effective indices and propagation lengths of the two modes for $t_3 > 30$ nm and $t_3 > 70$ nm, respectively. Again, this is a result of the dwindling field penetration through the Ag film, which implies that any further increase in its thickness tends to have a less-significant influence on modes until their propagation parameters settle at their final values. In addition, it is obvious from Fig. 4 that the maximum propagation length of TM_0 is much less than that of TE_0 (~40% smaller with the given simulation parameters), and consequently the sensing interactive length is constrained not to exceed the former (i.e., $L \leq L_{p,TM_0}$). It should be mentioned that the proposed interferometer in this work is designed with $t_3 = 90$ nm because we have found that this thickness is sufficient to ensure that L_{p,TM_0} reaches a maximum regardless of the Si core and spacer thicknesses that will be adjusted later to achieve the desired sensitivity.

B. Effect of Modes' Effective Indices Sensitivities on Interferometer Sensing Capability

An insight into Eq. (1) shows that the sensitivities of TM_0 and TE_0 effective indices versus RI variations in the sensing medium (the two terms inside brackets) play a substantial role in the function of the proposed interferometer. Overall, the HPWG should be designed so that TM_0 has a high sensitivity, as being a sensing mode, relatively to the reference mode TE_0 that is minimally affected by weak RI perturbations in the sensing medium. In this way, the difference between these two sensitivities is extended, which helps enhance the interferometer sensitivity.

Accordingly, the influence of changing thicknesses of the Si core and spacer on the effective indices sensitivities is explored to examine this criterion. The modal characteristic equations are solved over a wide thickness range of the Si core t_1 and spacer t_2 to find the corresponding values of the effective indices sensitivities defined by the derivatives $\frac{\partial n_{eff,TM_0}}{\partial n_s}$ and $\frac{\partial n_{eff,TE_0}}{\partial n_s}$ at the neighborhood of the unperturbed sensing medium RI ($n_s' = 1.33$), which are then depicted by the color maps in Figs. 5(a) and 5(b), respectively. In this simulation, the Ag film thickness t_3 is kept fixed at 90 nm. Interestingly, we notice a significant difference between the sensitivity levels of the effective indices of the two modes as the Si core and spacer thicknesses vary. Overall, TM_0 exhibits a much higher sensitivity than TE_0, which is approximately fivefold. Further, since TM_0 is a hybrid mode, increasing either t_1 or t_2 causes the field of that mode to be redistributed in the Si core as well as the spacer. Consequently, the sensitivity of the TM_0 effective index shown in Fig. 5(a) varies its value according to the electromagnetic field intensity inside and in the neighborhood of the sensing medium (spacer); the more intense the field, the higher the sensitivity. Sensitivity peaks (areas with reddish color) indicate the values of t_1 and t_2 at which the sensing mode TM_0 is most affected by weak RI perturbations in the sensing medium. However, TE_0 is a lossy mode that has most of its field inside the Si core, as illustrated by the polarization spatial diversity concept presented in Fig. 2. Consequently, increasing t_1 provides more separation between the sensing medium and the field of that mode since it becomes more confined inside the Si core. Accordingly, its effective index sensitivity declines gradually, as revealed from Fig. 5(a), manifesting that the reference mode TE_0 is less influenced by RI variations in the sensing medium. In contrast, increasing t_2 means that the sensing medium is wider, and consequently more TE_0 evanescent field extends through it, which contributes to the marginal increase in TE_0 effective index sensitivity noted on the same figure.

One might suggest that extending the sensitivity difference between the effective indices of the two modes to the maximum limit is sufficient to achieve the ultimate sensing capability; however, the sensing interactive length also should be taken into account. Here, our calculations are carried out with the assumption that $L = L_{p,TM_0}$. Thus, it is reasonable to state that L increases by increasing either t_1 or t_2 because the hybrid mode TM_0 is tending to be less influenced by the Ag film, and, consequently, has a more dielectric nature. Meanwhile, this comes at the expense of reducing the difference between the sensitivities of the two modes, as can be observed by comparing Figs. 5(a) and 5(b).

Accordingly, to design the interferometer with an appropriate sensitivity, we multiply L by $\left(\frac{\partial n_{eff,TM_0}}{\partial n_s} - \frac{\partial n_{eff,TE_0}}{\partial n_s}\right)$ and plot the product that represents the figure of merit (FOM), indicating the interferometer sensitivity according to Eq. (1), over a wide range of t_1 and t_2 in Fig. 6. Surprisingly, it is obvious that the interferometer sensitivity changes are dominated by L rather

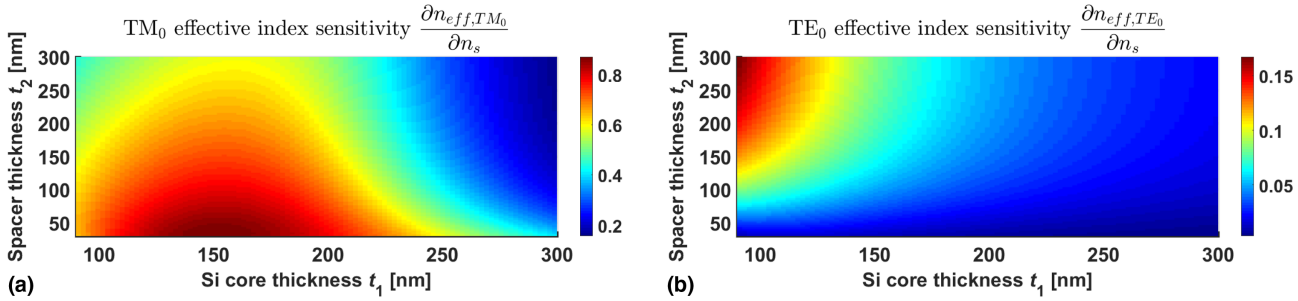

Fig. 5. Effective index sensitivity with sweeping Si core thickness t_1 and spacer thickness t_2 for (a) TM_0 and (b) TE_0.

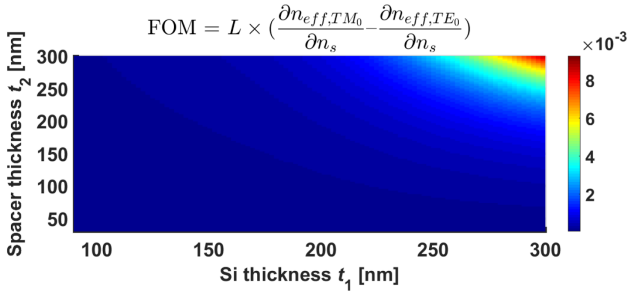

Fig. 6. Interferometer FOM with sweeping Si core thickness t_1 and spacer thickness t_2.

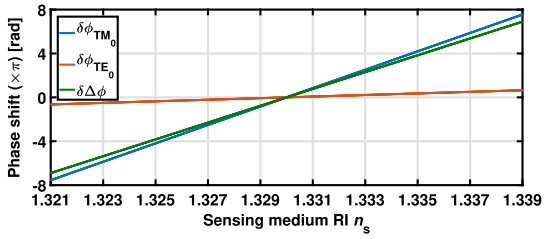

Fig. 7. TM_0 and TE_0 phase shifts; shift in their phase difference versus sensing medium RI n_s.

Table 1. Propagation Parameters of Modes in the HPWG Difference Interferometer

Mode	β [rad/μm]	Γ [dB/μm]	L_p [μm]	$\frac{\partial n_{eff}}{\partial n_s}$
TM_0	$8.248 + j3.582 \times 10^{-4}$	3.111×10^{-3}	1396	0.466
TE_0	$11.500 + j6.937 \times 10^{-5}$	6.025×10^{-4}	7208	0.040

than $\left(\frac{\partial n_{\text{eff,TM}_0}}{\partial n_s} - \frac{\partial n_{\text{eff,TE}_0}}{\partial n_s}\right)$ because it follows the same tendency of the former; the thicker the Si core and the spacer, the higher the interferometer sensitivity. Thus, one can conclude that $\frac{\partial n_{\text{eff,TM}_0}}{\partial n_s}$ and $\frac{\partial n_{\text{eff,TE}_0}}{\partial n_s}$ have little fluctuations over the $t_1 t_2$ plane with respect to L. That is why the areas of a high FOM shown in Fig. 6 do not coincide with those of remarkable difference between Figs. 5(a) and 5(b). Here, we assume an equal thickness of 220 nm for both t_1 and t_2 as a compromise between the high sensitivity and the short sensing interactive length, as will be shown through the following results. In addition, this value is typically provided for the Si core in standard SOI wafers. Indeed, higher interferometer sensitivities are still achievable by further thickening both the Si core and spacer to increase TM_0 propagation length, as discussed above. But this comes at the expense of increasing the sensing interactive length.

To summarize, Table 1 provides the calculated modal propagation parameters for the proposed design of the HPWG difference interferometer.

C. Evaluating Interferometer Sensitivity

Considering the aforementioned design, we examine the performance of the proposed interferometer. By introducing weak perturbations into the RI of the sensing medium, the generated phase shift of each polarization, along with the resulting shift in their phase difference, are calculated through Eq. (1) and displayed in Fig. 7. It is evident that, in spite of the significant phase shift of TM_0 that varies linearly versus n_s with a gradient of about 826.9π rad/RIU (the blue line), the TE_0 phase shift is relatively small with a gradient of only 70.6π rad/RIU (the red line), which is less than one-tenth of the former. Thus, the primary functional requirement of the HPWG difference interferometer is met. By calculating the gradient of the phase difference shift shown in Fig. 7 (the green line), the interferometer sensitivity is obtained to be 756.2π rad/RIU. The LOD can also be determined according to the minimum phase difference that can be measured experimentally. Considering a measurement precision of $2\pi \times 5 \times 10^{-4}$ rad [23], the LOD of the proposed interferometer is calculated to be 1.32×10^{-6} RIU.

Table 2 introduces a brief comparison between our HPWG difference interferometer and other single-path interferometers reported in the literature. An insight shows that our results obtained in this work outweigh those previously reported for all-dielectric interferometers in terms of the sensitivity, LOD, and sensing interactive length. When compared to the SOI-based two-lateral-modes spiral waveguide interferometer reported in [32], our proposed interferometer achieves an improvement in sensitivity by about 64%, besides a reduction in sensing interactive length by more than threefold, using a straight HPWG. Yet, the LOD of the latter is 10 times more precise. Furthermore, the polymer-based BiMW interferometer introduced in [33] is shown to achieve less than half the sensitivity of our device. Nevertheless, its sensing interactive length is longer by 72%. Despite the high sensitivity attained by the Si_3N_4-based BiMW interferometer in [31], its sensing interactive length is much longer than obtained in this work by roughly tenfold (15 mm). However, the same sensitivity (4052π rad/RIU) can be obtained using our device by altering

Table 2. Comparison between Various Single-Path Interferometers

		L [μm]	Γ [dB/μm]	$\frac{\partial\Delta\phi}{\partial n_s}$ [rad/RIU]	LOD [RIU]
Our work	SOI-based HPWG difference interferometer	1396	3.11×10^{-3}	756.2π	1.32×10^{-6}
[32]	SOI-based two-lateral-modes spiral waveguide interferometer	4582 (spirally folded)	–	461.6π	2.2×10^{-5}
[33]	Polymer-based BiMW interferometer	5000	–	316π	–
[31]	Si_3N_4-based BiMW interferometer	15,000	–	4052π	2.5×10^{-7}
[34]	SOI-based surface plasmon interferometer	10	1.79	–	$\sim 10^{-6}$

the waveguide design so that $t_1 = 250$ nm and $t_2 = 300$ nm. In this case, the TM_0 propagation loss is lessened from that value mentioned in Table 1 to 3.744×10^{-4} dB/μm, allowing an increase in the sensing interactive length to be 11.6 mm, which is still shorter by 22.7% than that reported in [31]. Indeed, this is considered an advantage of HPWGs: the ability to flexibly tune the sensing interactive length to achieve the desired sensitivity while maintaining an invariably low propagation loss as the condition $L = L_{p,TM_0}$ is preserved.

On the other hand, the surface plasmon interferometer proposed in [34] is designed with a very short length (10 μm), achieving a LOD comparable to that of our device ($\sim 10^{-6}$ RIU). However, because of the strong electromagnetic power dissipation in plasmonic devices, it suffers from an excessive propagation loss (1.79 dB/μm) that exceeds the calculated loss in this work by more than 5×10^2 times. Indeed, the higher the propagation loss, the lower the power level to be detected. When this happens, special optical detectors of a higher precision are subsequently required. Based on the presented figures of the sensing interactive lengths as well as the propagation losses, and assuming an input power level of 0 dBm, we can estimate the output power level of our HPWG difference interferometer to be −4.3 dBm, compared to 17.9 dBm using the previously reported surface plasmon interferometer.

The light interference intensity $I(\lambda_c)$ is obtained by evaluating Eq. (11) at a fixed wavelength λ_c over the range of n_s introduced in Fig. 7. In Fig. 8, we illustrate the normalized intensity $I_n(\lambda_c)$, where $I_n(\lambda_c) = I(\lambda_c)/I_0(\lambda_c)$. It is obvious that the generated shift in phase difference causes light intensity to be modulated, depending on sensing medium RI variation. However, approaching the points of local extrema in Fig. 8, changes in the interference intensity versus the weak RI perturbations undergo fading as $\frac{\partial I(\lambda_c)}{\partial n_s} \to 0$; that is, small values of δn_s will generate slight intensity changes $\delta I(\lambda_c)$. Further, at these points, there is an ambiguity in determining whether the variation in n_s is positive or negative. Apparently, the sensing functionality depends on the operating point (the value of n_s). Indeed, this restricts the dynamic range of the interferometer [18].

The problems of fading and ambiguity can be overcome by resolving the interferometer's response directly through the time-dependent phase difference $\Delta\phi$. In this case, though, a relatively complex scheme is required for proper detection, as introduced in [24]. Alternatively, the interferometer can be interrogated by a broadband source to have the interferometer's response resolved through spectral shifts in the wavelength domain.

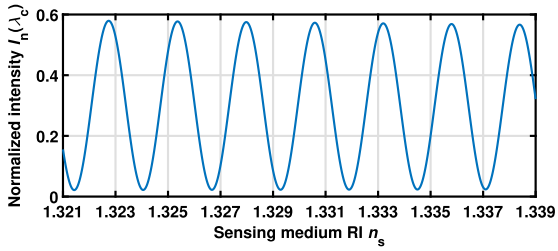

Fig. 8. Normalized intensity at the central operating wavelength λ_c versus sensing medium RI n_s.

D. Broadband HPWG Difference Interferometer

Next, we investigate our proposed HPWG difference interferometer when illuminated by a broad-spectrum light. The waveguide layers' thicknesses are kept at the design values obtained above (t_1, $t_2 = 220$ nm, and $t_3 = 90$ nm). The wavelength-dependent RI of the Ag film $n_4(\lambda)$ is taken from [35].

As shown by Eqs. (2) and (3), the broadband sensing functionality is essentially influenced by the dispersion functions $\beta_{TM_0}(\lambda)$ and $\beta_{TE_0}(\lambda)$. Accordingly, we solve the modal characteristic equations, as described in Section 3, for a relatively wide range of wavelengths (from 1490 to 1610 nm), assuming that $n_s = n_s'$. The corresponding real and imaginary parts of $\beta_{TM_0}(\lambda)$ and $\beta_{TE_0}(\lambda)$ are displayed in Fig. 9. Evidently, one can notice that both $\Re\{\beta_{TM_0}(\lambda)\}$ and $\Re\{\beta_{TE_0}(\lambda)\}$ decline as λ increases, indicating less confinement of the two modes in the guiding layer (Si core) because the ratio t_1/λ is getting smaller. As a consequence, the two modes have more electromagnetic power leakage from the Si core into the spacer, and become more influenced by the Ag film. Accordingly, both $\Im\{\beta_{TM_0}(\lambda)\}$ and $\Im\{\beta_{TE_0}(\lambda)\}$ grow, resulting in more absorptive losses, and consequently shorter propagation lengths, according to Eqs. (14) and (15). However, we notice that $\Im\{\beta_{TM_0}(\lambda)\}$ is more influenced by changes in λ than $\Im\{\beta_{TE_0}(\lambda)\}$. This is due to the polarization spatial diversity feature presented in Fig. 2, which renders the propagation loss of TM_0 more sensitive to the changes in its electromagnetic field distribution than that of TE_0.

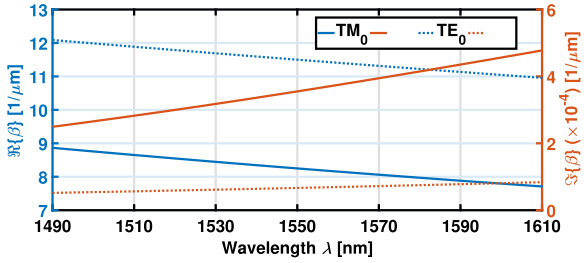

Fig. 9. Dispersion functions of TM_0 and TE_0.

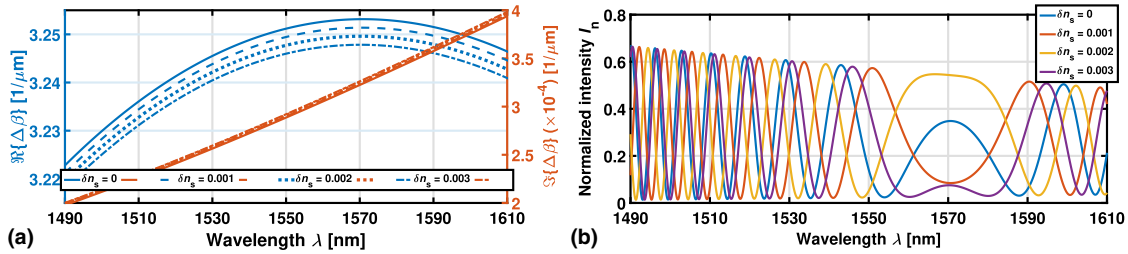

Fig. 10. (a) Dispersion difference function and (b) normalized intensity for various RI variations δn_s.

To demonstrate the light intensity produced by the two interfering modes, we first depict $\Re\{\Delta\beta(\lambda)\}$ and $\Im\{\Delta\beta(\lambda)\}$ in Fig. 10(a). Next, we make use of Eq. (2) to calculate the light interference intensity at different values of δn_s (0.001, 0.002, and 0.003). After that, we plot its normalized version $I_n(\lambda)$ in Fig. 10(b), where $I_n(\lambda) = I(\lambda)/I_0(\lambda)$. Here, the sensing interactive length is kept fixed at its value obtained above for the central operating wavelength when the sensing medium is unperturbed ($L = 1396\ \mu$m). As both L_{p,TM_0} and L_{p,TE_0} change values while sweeping the different wavelengths, it should be remarked that the previously imposed condition that $L = L_{p,TM_0}$ no longer holds in the broadband analysis.

In Eq. (2), $\frac{\partial\Re\{\Delta\beta\}}{\partial\lambda}$ determines the pitch at which the light interference intensity changes over wavelengths through the cos(·) term. Accordingly, the regions that exhibit a higher gradient of $\Re\{\Delta\beta(\lambda)\}$ in Fig. 10(a) (the blue curves) correspond to a faster-varying intensity pattern in Fig. 10(b). In addition, $\Im\{\Delta\beta(\lambda)\}$ introduces a positive displacement to the whole spectrum through the cosh(·) term in Eq. (2). This displacement can be easily seen by noticing the positions of the local minima of the spectrum in Fig. 10(b), which are slightly deviated above zero. Obviously, the deviation amount increases with increasing λ, following $\Im\{\Delta\beta(\lambda)\}$ that also builds up at higher wavelengths, as shown by Fig. 10(a) (red curves). Further, because of the absorptive loss induced by the Ag film in the HPWG, the local maxima of the normalized spectrum do not reach unity, which is different from the all-dielectric broadband difference interferometers reported in [29,30]. Instead, the nonzero $\Im\{\beta_{TM_0}(\lambda)\}$ and $\Im\{\beta_{TE_0}(\lambda)\}$ cause the initial intensity distributive function $I_0(\lambda)$ to be attenuated monotonically by the exponential factor in Eq. (2). It is worth noticing the agreement between the direction of increasing either $\Im\{\beta_{TM_0}(\lambda)\}$ or $\Im\{\beta_{TE_0}(\lambda)\}$ in Fig. 9, and that of increasing attenuation of the normalized intensity in Fig. 10(b).

The wavelength shift of a local extremum existing at a wavelength λ_m in the spectrum is estimated through Eq. (3), for different values of δn_s, and displayed in Fig. 11. The numerator of Eq. (3) $\frac{\partial\Re\{\Delta\beta\}}{\partial n_s}$ is a negative value, as can be remarked from Fig. 10(a). This is because increasing spacer RI n_s boosts the n_{eff} of all guided modes in the Si core below it, specified by Eq. (13), which leads to an increase in their corresponding real part of β, according to Eq. (14). However, since TM_0 has a greater field in the sensing region (spacer) than TE_0, as illustrated by Fig. 2, the former has a higher sensitivity to weak RI perturbations in the sensing medium. Accordingly, while n_s increases, $\Re\{\beta_{TM_0}(\lambda)\}$ approaches $\Re\{\beta_{TE_0}(\lambda)\}$, and the difference $\Re\{\Delta\beta(\lambda)\}$ declines.

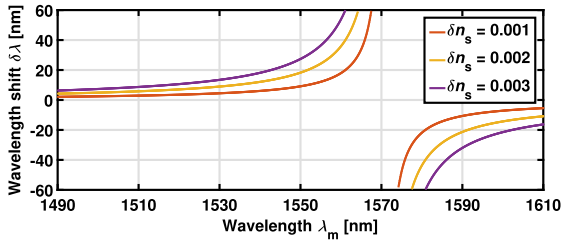

Fig. 11. Wavelength shift of a local extremum with sweeping wavelength λ_m for various RI variations δn_s.

Meanwhile, the sign of the denominator $\frac{\partial\Re\{\Delta\beta\}}{\partial\lambda}$ determines the direction of wavelength shift. In other words, the wavelengths of a positive slope in Fig. 10(a) (the blue curves) correspond to a red-shift ($\delta\lambda > 0$) in Fig. 11, whereas a blue-shift ($\delta\lambda < 0$) coexists with the wavelengths of a negative slope. However, there is a certain narrow band of wavelengths at which the shift cannot be identified properly because of the vanishing denominator of Eq. (3). These wavelengths coincide with the flat regions in Fig. 10(a) (the blue curves), where $|\delta\lambda|$ exhibits a sharp increase before undergoing a discontinuity (Fig. 11).

The broadband sensing functionality is accomplished by tracking red- and blue-shifts in λ_m occurring over time. We make use of Eq. (3) to evaluate the sensitivity $|\frac{\partial\lambda}{\partial n_s}|$ at λ_c. As $\frac{\partial\lambda}{\partial n_s} \propto \frac{\partial\Re\{\Delta\beta\}}{\partial n_s}$, the sensitivity is found to be as high as 9.118×10^3 nm/RIU thanks to the remarkable difference between the effective indices sensitivities of TM_0 and TE_0 in HPWGs (see Table 1).

It has been shown in [18] that the more the points of local extrema in the spectral range of interest, the more accurately the interference intensity signal can be statistically analyzed. Interestingly, when compared to the all-dielectric broadband difference interferometers reported in [29,30], the advantage introduced by the broadband HPWG difference interferometer is the relatively high density of local extrema in the investigated spectral range, as evident from Fig. 10(b), despite its short length (1396 μm). This merit of our device arises thanks to the distinctive distribution of the dispersion difference function $\Re\{\Delta\beta(\lambda)\}$ shown in Fig. 10(a), which has a greater averaged inclination over the investigated spectral range. Indeed, this contributes to increase the frequency at which the light interference intensity in Eq. (2) swings between local maxima and minima, without the need to increase the sensing interactive length.

5. CONCLUSION

We have investigated an SOI HPWG as a difference interferometer RI sensor. A rigorous analytical model has been provided to explore how the distinct modal features of TM and TE polarizations in HPWGs can be exploited by the sensing mode TM_0 and the reference mode TE_0 propagating through the same waveguide to achieve the ultimate sensing capability. Aside from its simple structure, since no vertical nor horizontal discontinuous junctions are needed as in the case of BiMW interferometers, our HPWG difference interferometer exhibits an unprecedented combination of the high RI sensitivity, the short sensing interactive length, and the low propagation loss. Specifically, the sensitivity has been shown to be 756.2π rad/RIU with a highly precise LOD (1.32×10^{-6}) achieved at a wavelength of 1550 nm through an interactive length as short as 1396 μm; the figures that have been found to be premium compared with previously reported single-path interferometers using all-dielectric waveguides. Moreover, the propagation loss in our work has been calculated to be 3.11×10^{-3} dB/μm, compared to 1.79 dB/μm using an SOI-based surface plasmon interferometer proposed in the literature, which makes the optical detection simpler with our interferometer because of the higher level of received power. Furthermore, we have investigated the proposed interferometer with a broadband illumination ranging from 1490 to 1610 nm to avoid the problems of ambiguous detection as well as fading of the interferometric signal, which may be faced with the single-wavelength interrogation. Despite the short sensing interactive length, the broadband analysis has revealed a dense allocation of interference intensity local extrema, which is deemed an additional advantage of our device. Although we have considered a slab HPWG in this work to provide an exact modal analysis based on a firm mathematical model, the obtained findings may motivate further research to extend the proposed idea to strip or rib HPWGs, based on numerical finite-difference time-domain simulation methods.

Disclosures. The authors declare no conflicts of interest.

Data Availability. Data underlying the results presented in this paper are not publicly available at this time but may be obtained from the authors upon reasonable request.

REFERENCES

1. M. J. Deen and P. K. Basu, *Silicon Photonics: Fundamentals and Devices* (Wiley, 2012), Vol. **44**.
2. D. Inniss and R. Rubenstein, *Silicon Photonics: Fueling the Next Information Revolution* (Morgan Kaufmann, 2016).
3. X. C. Tong, *Advanced Materials for Integrated Optical Waveguides*, Vol. **46** (Springer, 2014),.
4. H. Ditlbacher, J. R. Krenn, G. Schider, A. Leitner, and F. R. Aussenegg, "Two-dimensional optics with surface plasmon polaritons," Appl. Phys. Lett. **81**, 1762–1764 (2002).
5. S. Hayashi and T. Okamoto, "Plasmonics: visit the past to know the future," J. Phys. D **45**, 433001 (2012).
6. S. A. Maier, *Plasmonics: Fundamentals and Applications* (Springer, 2007).
7. L. Thylen, P. Holmström, L. Wosinski, B. Jaskorzynska, M. Naruse, T. Kawazoe, M. Ohtsu, M. Yan, M. Fiorentino, and U. Westergren, "Nanophotonics for low-power switches," in *Optical Fiber Telecommunications VIA* (Elsevier, 2013), Chap. 6.
8. Y. Fang and M. Sun, "Nanoplasmonic waveguides: towards applications in integrated nanophotonic circuits," Light Sci. Appl. **4**, e294 (2015).
9. R. F. Oulton, V. J. Sorger, D. A. Genov, D. F. P. Pile, and X. Zhang, "A hybrid plasmonic waveguide for subwavelength confinement and long-range propagation," Nat. Photonics **2**, 496–500 (2008).
10. Z. Han and S. I. Bozhevolnyi, "Radiation guiding with surface plasmon polaritons," Rep. Prog. Phys. **76**, 016402 (2012).
11. M. Alam, J. Meier, J. Aitchison, and M. Mojahedi, "Super mode propagation in low index medium," in *Quantum Electronics and Laser Science Conference* (Optical Society of America, 2007), paper JThD112.
12. M. Z. Alam, J. S. Aitchison, and M. Mojahedi, "A marriage of convenience: Hybridization of surface plasmon and dielectric waveguide modes," Laser Photon. Rev. **8**, 394–408 (2014).
13. M. Alam, "Hybrid plasmon waveguides: theory and applications," Ph.D. thesis (University of Toronto, 2012).
14. M. Alam, J. S. Aitchison, and M. Mojahedi, "Theoretical analysis of hybrid plasmonic waveguide," IEEE J. Sel. Top. Quantum Electron. **19**, 4602008 (2013).
15. R. Salvador, A. Martinez, C. Garcia-Meca, R. Ortuno, and J. Marti, "Analysis of hybrid dielectric plasmonic waveguides," IEEE J. Sel. Top. Quantum Electron. **14**, 1496–1501 (2008).
16. M. T. Noghani and M. H. V. Samiei, "Analysis and optimum design of hybrid plasmonic slab waveguides," Plasmonics **8**, 1155–1168 (2013).
17. P. Kozma, F. Kehl, E. Ehrentreich-Förster, C. Stamm, and F. F. Bier, "Integrated planar optical waveguide interferometer biosensors: A comparative review," Biosens. Bioelectron. **58**, 287–307 (2014).
18. M. Kitsara, K. Misiakos, I. Raptis, and E. Makarona, "Integrated optical frequency-resolved Mach-Zehnder interferometers for label-free affinity sensing," Opt. Express **18**, 8193–8206 (2010).
19. K. Misiakos, I. Raptis, A. Salapatas, E. Makarona, A. Botsialas, M. Hoekman, R. Stoffer, and G. Jobst, "Broad-band Mach-Zehnder interferometers as high performance refractive index sensors: Theory and monolithic implementation," Opt. Express **22**, 8856–8870 (2014).
20. K. Misiakos, I. Raptis, E. Makarona, A. Botsialas, A. Salapatas, P. Oikonomou, A. Psarouli, P. Petrou, S. Kakabakos, K. Tukkiniemi, M. Sopanen, and G. Jobst, "All-silicon monolithic Mach-Zehnder interferometer as a refractive index and bio-chemical sensor," Opt. Express **22**, 26803–26813 (2014).
21. X. Sun, D. Dai, L. Thylén, and L. Wosinski, "High-sensitivity liquid refractive-index sensor based on a Mach-Zehnder interferometer with a double-slot hybrid plasmonic waveguide," Opt. Express **23**, 25688–25699 (2015).
22. M. Alam, F. Bahrami, J. Aitchison, and M. Mojahedi, "Analysis and optimization of hybrid plasmonic waveguide as a platform for biosensing," IEEE Photon. J. **6**, 3700110 (2014).
23. W. Lukosz, C. Stamm, H. Moser, R. Ryf, and J. Dübendorfer, "Difference interferometer with new phase-measurement method as integrated-optical refractometer, humidity sensor and biosensor," Sens. Actuators B Chem. **39**, 316–323 (1997).
24. W. Lukosz and C. Stamm, "Integrated optical interferometer as relative humidity sensor and differential refractometer," Sens. Actuators A Phys. **25**, 185–188 (1990).
25. C. Stamm and W. Lukosz, "Integrated optical difference interferometer as refractometer and chemical sensor," Sens. Actuators B Chem. **11**, 177–181 (1993).
26. C. Fattinger, H. Koller, D. Schlatter, and P. Wehrli, "The difference interferometer: a highly sensitive optical probe for quantification of molecular surface concentration," Biosens. Bioelectron. **8**, 99–107 (1993).
27. K.-I. Tsunoda, S. Kikuchi, K. Nomura, K. Aizawa, K. Okamoto, and H. Akaiwa, "Characteristics of sensor response of a difference interferometric slab optical waveguide refractive index sensor with a prism coupling method," Anal. Sci. **15**, 241–247 (1999).
28. W. Lukosz, "Integrated optical chemical and direct biochemical sensors," Sens. Actuators B Chem. **29**, 37–50 (1995).
29. K. Gut, "Broad-band difference interferometer as a refractive index sensor," Opt. Express **25**, 31111–31121 (2017).

30. K. Gut, "Study of a broadband difference interferometer based on low-cost polymer slab waveguides," Nanomaterials (Basel) **9**, 729 (2019).
31. K. E. Zinoviev, A. B. González-Guerrero, C. Domínguez, and L. M. Lechuga, "Integrated bimodal waveguide interferometric biosensor for label-free analysis," J. Lightwave Technol. **29**, 1926–1930 (2011).
32. Q. Liu, K. W. Kim, Z. Gu, J. S. Kee, and M. K. Park, "Single-channel Mach-Zehnder interferometric biochemical sensor based on two-lateral-mode spiral waveguide," Opt. Express **22**, 27910–27920 (2014).
33. Y. Liang, M. Zhao, Z. Wu, and G. Morthier, "Bimodal waveguide interferometer RI sensor fabricated on low-cost polymer platform," IEEE Photon. J. **11**, 6801108 (2019).
34. P. Debackere, S. Scheerlinck, P. Bienstman, and R. Baets, "Surface plasmon interferometer in silicon-on-insulator: novel concept for an integrated biosensor," Opt. Express **14**, 7063–7072 (2006).
35. S. Babar and J. Weaver, "Optical constants of Cu, Ag, and Au revisited," Appl. Opt. **54**, 477–481 (2015).
36. H. A. Okda, E. A. Elzahaby, I. Kandas, M. H. Aly, and M. El Osairy, "Plasmonic enhancement to second-order nonlinearity in optical fibers," J. Lightwave Technol. **36**, 4834–4842 (2018).